Amorphous quaternary alloy nanoplates for efficient catalysis of hydrogen evolution reaction

Qianyun Bai[a], Xiaoxiao Yan[a], Da Liu[a], Kang Xiang[a], Xin Tu[b,*], Yanhui Guo[a,*], Renbing Wu[a,*]

[a]*Department of Materials Science, Fudan University, Shanghai 200438, China*

[b]*Department of Electrical Engineering and Electronics, University of Liverpool, Liverpool L69 3GJ, UK*

*E-mail addresses: xin.tu@liverpool.ac.uk (X. Tu); gyh@fudan.edu.cn (Y. Guo); rbwu@fudan.edu.cn (R. Wu)

Abstract

Developing a highly efficient non-precious transition metal-based electrocatalyst via a facile approach toward the hydrogen evolution reaction (HER) is critical for large-scale hydrogen production but still remains challenging. Herein, a cost-effective electrochemical deposition strategy is rationally proposed to construct amorphous quaternary FeCoNiCu alloy nanosheets supported on nickel foam (NF) towards this challenge. Benefiting from the synergistic effect of multi-metal atoms interaction and the high exposure of active sites caused by abundant open voids, the as-synthesized FeCoNiCu/NF electrode exhibits high catalytic activity and robustness toward HER in alkaline solution, requiring an overpotential of only 35 mV to reach a current density of 10 mA cm^{-2}. This study may pave a new avenue to design advanced electrocatalyst for energy conversion.

1. Introduction

Molecular hydrogen (H_2), featured by high energy density and environmental friendliness, has been deemed as a clean energy carrier to substitute traditional fossil fuels [1,2]. Electrochemical water splitting provides a sustainable way to generate hydrogen fuel via the conversion and storage of renewable energy [3–5]. Compared with the expensive acid proton-exchange membrane (PEM) water electrolyzers that

need precious metal-based electrode, alkaline water electrolyzers using earth-abundant transition metal-based catalysts may be more promising for realizing the mass commercialization of hydrogen production [6–9]. However, the sluggish kinetics derived from the additional energy barrier of water dissociation still hinder the further development of alkaline water splitting. Therefore, exploring highly efficient HER electrocatalysts with accelerated kinetics is urgently demanded [10,11].

3d transition metals-based materials are one of the most promising candidates due to their abundant resources and benign electrocatalytic activity [12,13]. In particular, alloying individual metallic elements to form alloys with two or more compositions is considered as an effective way to further extensively enhance their intrinsic activity. In the past decades, a variety of binary, ternary, quaternary and high-entropy alloys have been successfully prepared for electrocatalytic HER [14–17]. Compared with the individual metal catalyst, the electronic structures of alloy catalysts with two or more metal compositions can be intensively modulated towards an optimized adsorption energy of intermediates involved in HER, thus exhibiting a remarkable catalytic activity.

Melt-alloying strategy and high-energy ball milling are usually employed to prepare transition metal alloys catalyst. For example, Jia et al. demonstrated that high-entropy intermetallic could be synthesized using melt-spinning technique under a high temperature and high-purity argon (Ar) atmosphere [18]. The FeCoNiAlTi alloy showed enhanced HER performance with an overpotential of 88.2 mV at a current density of 10 mA cm^{-2}. Ma et al. reported a synthesis of self-supported CoCrFeNiAl high-entropy alloy electrocatalyst via a ball milling and spark plasma sintering (SPS) consolidation process [19]. The electrocatalyst presented a favorable activity with an overpotential of 73 mV to reach a current density of 10 mA cm^{-2}. Notwithstanding

prominent achievements that have been made, the synthesis of transition metal alloy electrocatalysts involves a stringent experimental condition such as high temperature or pressure and special equipment, which severely impedes their practical applications [20–23]. Furthermore, the reported alloy electrocatalysts are generally in a large size and aggregated, which may not be favorable to the exposure of active sites and facile charge transfer, thus leading to a limited electrocatalytic performance. Therefore, exploring alloy electrocatalysts with high density active sites via a low cost and convenient method is highly desired but remains challenging.

In this work, we developed an ultra-thin sheet-like amorphous FeCoNiCu alloy supported on nickel foam (denoted as FeCoNiCu/NF) by a one-step electrochemical deposition approach as an efficient HER electrocatalyst in alkaline media. Benefiting from the advantages of the highly exposure of active sites, the synergistic effect of quaternary metals and the amorphous structure, the as-prepared FeCoNiCu/NF catalyst shows an exceptional performance with an overpotential of 35 mV at a current density of 10 mA cm^{-2}, and excellent electrochemical stability during long-term test.

2. Experimental section

2.1 Chemicals

Nickel-(II) chloride ($NiCl_2$, 99%), Iron-(II) chloride ($FeCl_2$, 99%), Cobaltous-(II) chloride ($CoCl_2$, 99%), Copper-(II) chloride ($CuCl_2$, 99%), Lithium chloride (LiCl, ≥99%), Dimethyl sulfoxide (DMSO), Potassium hydroxide (KOH, >99.9%) were purchased from Macklin without further purification. Deionized water was used in all experiments.

2.2 Synthetic procedures

A three-electrode system was used to conduct the electrochemical deposition

experiments in DMSO-LiCl electrolyte. The nickel foam (NF) with 1.5 cm × 2 cm geometric areas was ultrasonic in acetone for 20 minutes to remove the residual organic species. After being washed by deionized water, the NF was then cleaned by ultrasonic for 20 minutes in 1 M HCl to eliminate the oxides and contamination on the surface, washed with water and dried in the oven. The as-prepared NF was used as the working electrode. The graphite and saturated calomel electrode (SCE) were used as the counter and reference electrode, respectively. $NiCl_2$ (0.002 M), $FeCl_2$ (0.002 M), $CoCl_2$ (0.002 M), $CuCl_2$ (0.002 M) and LiCl (0.25 M) were dissolved in DMSO to form the electrolyte. FeCoNiCu/NF would be finally obtained after experiencing the electrochemical deposition process at −2.3 V (vs. SCE) for 20 min. For comparison, Fe/NF, FeCo/NF and FeCoNi/NF were prepared using similar methods except that only the corresponding solvents were involved.

2.3 Characterizations

The morphologies and microstructures of the as-synthesized catalysts were characterized by field-emission scanning electron microscopy (FESEM, Ultra 55) and high-resolution transmission electron microscopy (HRTEM, FEI TalosF200x), respectively. The thickness of nanosheets was determined by atomic force microscopy (AFM, Bruker Dimension Icon). The phase structures were examined by powder X-ray diffraction (XRD, D8V Advance). The elemental distributions were characterized by energy-dispersive X-ray spectroscopy (EDS, FEI TalosF200x, Super-X). The chemical states and surface compositions were analyzed by X-ray photoelectron spectroscopy (XPS, Thermo Scientific K-Alpha). The element content analysis was performed by inductively coupled plasma-optical emission spectrometry (ICP-OES, Agilent 5110).

2.4 Electrocatalytic measurements

The electrochemical experiments were carried out using a standard three-electrode system at a CHI 760E electrochemical analyzer (Shanghai, Chenhua Co.). The as-prepared samples, a saturated calomel electrode (SCE) and a graphite rod were used as the working electrode, reference electrode and counter electrode, respectively. All measured potentials were converted to reversible hydrogen electrode (RHE), according to the formula of $E_{RHE} = E_{SCE} + 0.059 \times pH + 0.2412$ V [24]. The polarization curves were received by performing linear sweep voltammetry (LSV) at the scan rate of 5 mV s^{-1} in N_2-saturated 1.0 M KOH. Before sweeping, cyclic voltammetry (CV) measurements were conducted at a scan rate of 50 mV s^{-1} to activate the surface. Tafel slopes were derived by plotting the overpotential against log (current density) from the linear region of the LSV curves. The values were calculated according to the equation: $\eta = b \times \log j + a$, where η is the overpotential, b is the value of Tafel slope and j is the current density. Electrochemical impedance spectroscopy (EIS) measurements were performed at a potential of −0.1 V (vs. RHE), with a frequency range from 0.01 Hz to 100 kHz. The steady-state activity was evaluated by chronoamperometry measurements. The specific electrochemical double-layer capacitance (C_{dl}) was performed to evaluate the electrochemical active surface area (ECSA). CV scans were performed at a potential range from 0.57 to 0.67 V (vs. RHE) at different scan rates of 20, 40, 60, 80 and 100 mV s^{-1}. C_{dl} value was calculated by plotting $\Delta j = (j_{cathodic} - j_{anodic})/2$ at 0.52 V (vs. RHE) against the scan rates.

3. Results and Discussion

The quaternary alloy supported on nickel foam was prepared through an electrochemical deposition route with the corresponding metal salts dissolved in DMSO as source, as schematically illustrated in Fig. 1a. Fe/NF, FeCo/NF and

FeCoNi/NF samples were also prepared as counterparts by a similar synthetic method. The morphology of the FeCoNiCu/NF sample was characterized by field-emission scanning electron microscopy (FESEM). As displayed in Fig. 1b and 1c, the surface of the nickel foam is uniformly covered by vertically aligned and interconnected FeCoNiCu porous nanosheets, forming abundant open voids which are benefit to the penetration of electrolyte and the bubble release [25]. The thickness of the FeCoNiCu nanosheets characterized by the atomic force microscope (AFM) is determined to be about 4 nm (Fig. S1, Supporting Information). Similar sheet-like morphologies could also be observed on the surface of contrast samples (Fig. S2, Supporting Information), suggesting the universality of the potentiostatic deposition method for synthesis of nanosheets. X-ray diffraction (XRD) technique was carried out to investigate the crystallinity of the as-synthesized samples. As shown in Fig. 1d, only three diffraction peaks located at 44.5°, 51.8° and 76.3° that can be assigned to the Ni (JCPDS no. 04-0850) from nickel foam could be observed in all samples, indicating the formation of amorphous structure for the as-prepared nanosheets. Carbon cloth-supported FeCoNiCu nanosheets (denoted as FeCoNiCu/CC) were also fabricated to eliminate the signal coverage by the nickel foam in XRD characterizations (Fig. S3a, Supporting Information). Similarly, only diffraction peaks attribute to carbon cloth could be observed in FeCoNiCu/CC (Fig. S3b, Supporting Information), further confirming the amorphous feature of the FeCoNiCu alloy.

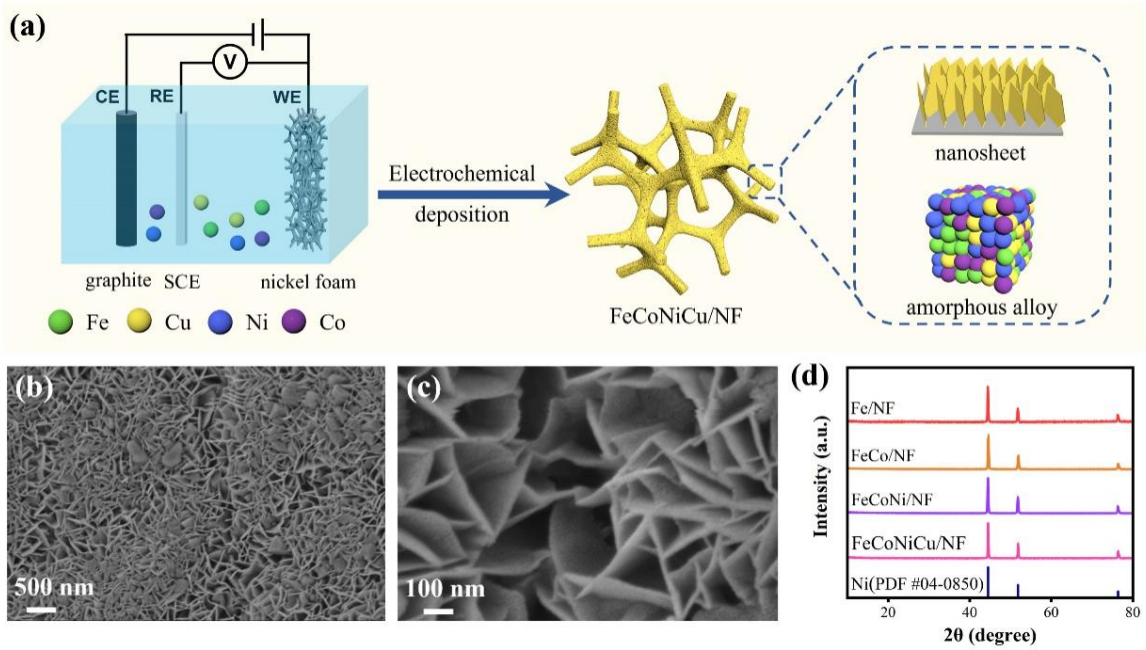

Fig. 1. (a) Schematic illustration of synthetic process of FeCoNiCu/NF. The WE, RE and CE refer to the working, reference, and counter electrode, respectively. (b, c) FESEM images of FeCoNiCu/NF at different magnifications. (d) XRD patterns of FeCoNiCu/NF, FeCoNi/NF, FeCo/NF and Fe/NF.

The microstructure of FeCoNiCu nanosheets was analyzed by transmission electron microscopy (TEM). As shown in Fig. 2a and 2b, the absence of lattice fringes as well as the ring-like characteristic of the selected area electron diffraction (SAED) pattern (inset in Fig. 2b) further verifies the amorphous phase of the sheet-like FeCoNiCu alloy. The scanning transmission electron microscope (STEM) image and the corresponding energy-dispersive spectroscopy (EDS) elemental mapping images (Fig. 2c) as well as the EDS spectrum (Fig. S4, Supporting Information) reveal the co-existence and evenly distribution of Fe, Co, Ni and Cu elements throughout the nanosheet, demonstrating the formation of a homogeneous phase. The contents of Fe, Co, Ni and Cu are determined to be 26.15%, 21.35%, 22.05% and 30.45% from the inductively coupled plasma optical emission spectrometer (ICP-OES), respectively,

which are close to the results from the EDS spectrum listed in Table S1. It could be found that the content of Cu is slightly higher than those of other metals, which might be attributed to the highest reduction potential of Cu [26].

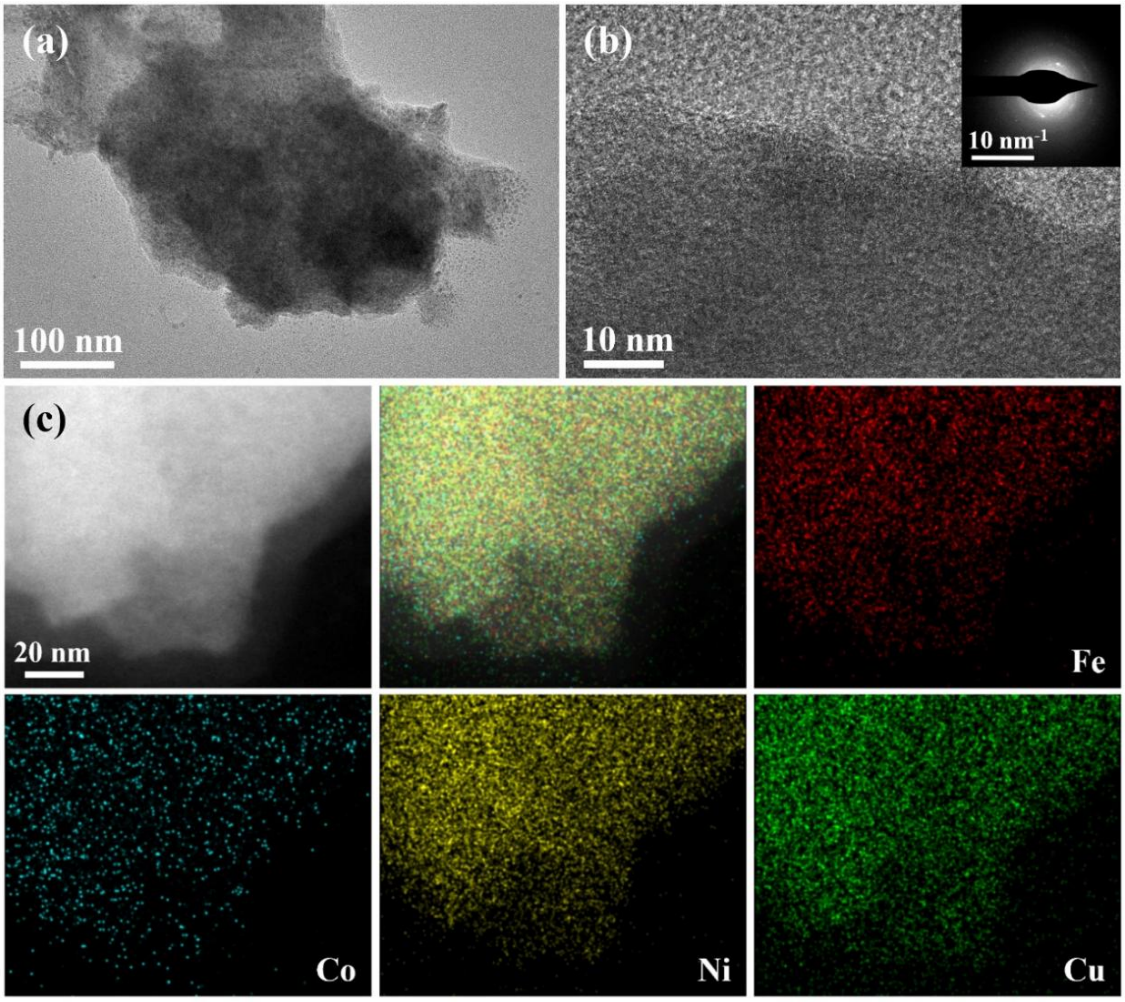

Fig. 2. (a) TEM image and (b) HRTEM image of the FeCoNiCu nanosheets. (c) STEM image and corresponding EDS elemental mapping images of the FeCoNiCu nanosheets. The inset in (b) is the SAED pattern.

According to empirical rules reported by Yang and Zhang [27], multiply-element alloy would form a stable phase if $\delta_r < 6.6\%$ and $\Omega = (T_m\Delta S_{mix})/|\Delta H_{mix}| > 1.1$, where δ_r is the difference in atomic radius, T_m is the melting temperature, ΔS_{mix} is the mixing entropy and ΔH_{mix} is the mixing enthalpy. The calculation results based on Formula 1–5 (Supporting Information) suggest that the value of δ_r (3.27%) and Ω (1.87) meet

the above-mentioned standard, indicating that the as-deposited alloy is theoretically considered to be a stable single phase [28,29]. Moreover, the mixing entropy (ΔS_{mix}) of FeCoNiCu alloy, FeCoNi alloy and FeCo alloy are calculated via Formula 6–9 (Supporting Information) with element contents determined by ICP-OES (Table 1–3, Supporting Information). ΔS_{mix} of the quaternary FeCoNiCu alloy is calculated to be 11.44 J K^{-1} mol^{-1}, which is higher than that of the ternary FeCoNi alloy (9.11 J K^{-1} mol^{-1}) and the binary FeCo alloy (5.74 J K^{-1} mol^{-1}), meaning an enhanced structural stability and durability [30–32].

To investigate the chemical composition and valence states of surface elements, X-ray photoelectron spectroscopy (XPS) was conducted. The XPS survey spectrum displayed in Fig. S5 (Supporting Information) indicates the presence of Fe, Co, Ni and Cu on the surface of the FeCoNiCu/NF sample, further verifying the successful formation of quaternary FeCoNiCu alloy. Fig. 3 shows the deconvoluted high-resolution Fe 2p, Co 2p, Ni 2p and Cu 2p XPS spectra, demonstrating the existence of oxide states in all elements. Specifically, the peaks located at 711.8 eV and 714 eV are attributed to metallic Fe^0 $2p_{3/2}$ and Fe^{2+} $2p_{3/2}$, respectively (Fig. 3a). The Co 2p XPS spectra in Fig. 3b could be deconvoluted into the characteristic peaks of Co^{2+} $2p_{3/2}$ (780.8 eV) and Co^{2+} $2p_{1/2}$ (798 eV). Similarly, for Ni 2p (Fig. 3c), the binding energies at 855.8 eV and 873.6 eV belong to the $2p_{3/2}$ and $2p_{1/2}$ of Ni^{2+}, respectively. The Cu 2p XPS spectra (Fig. 3d) display the co-existence of Cu^0 (932.3 eV) and Cu^{2+} (933.6 eV). Compared with FeCoNi ternary alloy, the 2p peaks of Fe and Co shift to lower binding energy while the 2p peaks of Ni shift to higher binding energy, possibly be due to the introduction of Cu (Fig. S6, Supporting Information). It is revealed that the introduction of Cu may play a significant effect on the electronic structure of the alloy. The positive shift of Ni^{2+} peak and the negative shift of the Co^{2+} and Fe^{2+}

related peaks in FeCoNiCu/NF compared to FeCoNi/NF prove that the synergy of quaternary alloy accelerates the charge transfer of the catalytic material and therefore facilitates the HER reaction.

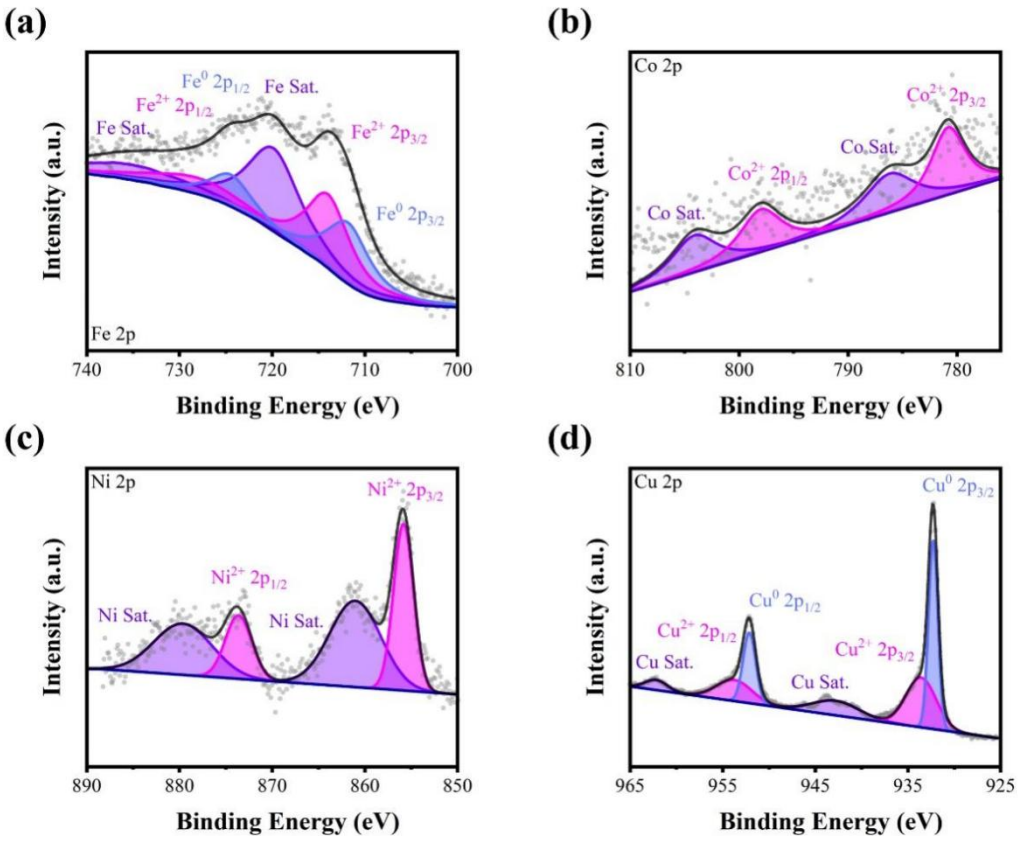

Fig. 3. High-resolution XPS spectra of FeCoNiCu/NF: (a) Fe 2p, (b) Co 2p, (c) Ni 2p and (d) Cu 2p.

The electrocatalytic HER performance of the as-synthesized FeCoNiCu/NF was evaluated in 1 M KOH solution using a three-electrode system. For comparison, FeCoNi/NF, FeCo/NF, Fe/NF, NF and commercial Pt/C samples were also measured under the same test condition. All potentials in this work were referenced to reversible hydrogen electrode (RHE) for convenience. Fig. 4a shows the liner scanning voltammetry (LSV) curves of all the samples measured in N_2-saturated 1 M KOH electrolyte with a scanning rate of 5 mV s^{-1} without *i*R compensation. The

FeCoNiCu/NF catalyst exhibits a low overpotential (η_{10}) of 35 ± 1 mV to deliver a current density of 10 mA cm^{-2}, which is much smaller than those observed in FeCoNi/NF (133 ± 2 mV), FeCo/NF (139 ± 2 mV), Fe/NF (148 ± 3 mV), NF (214 ± 2 mV) and commercial Pt/C (68 ± 1 mV) samples (Fig. 4b and Fig. S7 in Supporting Information). It is noteworthy that FeCoNiCu/NF still exhibits better electrocatalytic activity than Pt/C at a current density of 100 mA cm^{-2}. In particular, the catalytic activity of FeCoNiCu/NF also outperforms those of the recently reported non-precious transition metal-based electrocatalysts [33–45] (Fig. 4c and Table S4 in Supporting Information). Tafel plots (overpotential vs. log [current density]) displayed in Fig. 4d were derived to investigate the electrocatalytic kinetics and mechanisms of all the electrodes. The Tafel slope of FeCoNiCu/NF is identified to be 57 mV dec^{-1}, demonstrating a noticeably faster HER kinetic than those of FeCoNi/NF (108 mV dec^{-1}), FeCo/NF (126 mV dec^{-1}), Fe/NF (142 mV dec^{-1}) and NF (156 mV dec^{-1}) electrodes. The Tafel value of the FeCoNiCu/NF sample also indicates that the HER process might proceed by the Volmer-Heyrovsky mechanism [46]. Electrochemical impedance spectroscopy (EIS) was carried out to further examine the electrode kinetics of the HER process. The Nyquist plots in Fig. 4e could be well fitted by the equivalent circuit given in the inset. Compared with other counterparts, the FeCoNiCu/NF electrode exhibits the lowest charge transfer resistance (R_{ct}) value of 14.6 Ω, revealing the best charge transfer ability. The double-layer capacitance (C_{dl}) was employed to evaluate the active sites by measuring the non-Faradaic capacitive current using the cyclic voltammetry (CV) method with scanning rates from 20 to 100 $mV \cdot s^{-1}$ (Fig. S8, Supporting Information). As depicted in Fig. 4f, the C_{dl} value of FeCoNiCu/NF (5.58 mF cm^{-2}) surpasses those of FeCoNi/NF (1.81 mF cm^{-2}), FeCo/NF (1.60 mF cm^{-2}), Fe/NF (1.06 mF cm^{-2}) and NF (0.98 mF cm^{-2}), implying

that the amorphous structures coupled with randomly distributed atoms of four different elements are conducive to providing more exposed active sites and therefore enhancing HER activity.

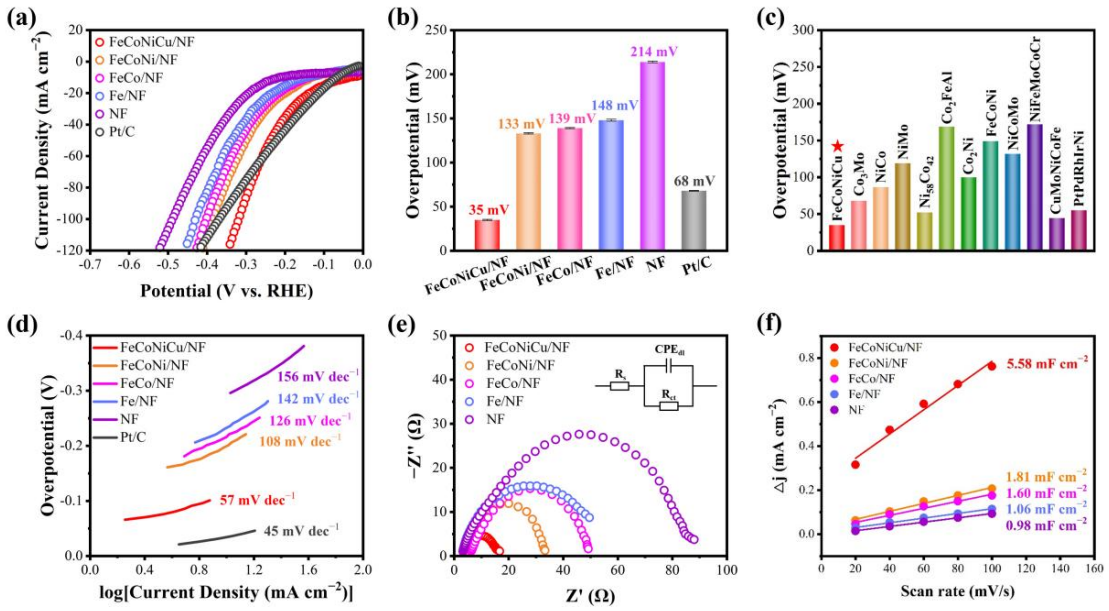

Fig. 4. Electrocatalytic tests of FeCoNiCu/NF, FeCoNi/NF, FeCo/NF, Fe/NF, pure NF and Pt/C for the HER in 1 M KOH solution: (a) LSV curves, (b) overpotentials at a current density of 10 mA cm^{-2}, (c) comparison of the overpotential of FeCoNiCu/NF at 10 mA cm^{-2} toward HER with other recently reported alloy catalysts, (d) Tafel plots, (e) Nyquist plots, (f) variation of double-layer charging current as a function of scanning rate.

Catalytic stability is another key parameter to evaluate the practical application potential of the catalyst. The chronoamperometry measurement was firstly conducted at a static overpotential when the current density reached 10 mA cm^{-2}. As shown in Fig. 5a, the FeCoNiCu/NF electrode exhibits negligible decay of current density during the stability test of 48 h, indicating the outstanding electrochemical stability. The LSV curves before and after the *i-t* test could also verify the fantastic stability

(Fig. 5b). In particular, the overpotential at 10 mA cm^{-2} increases by only 21 mV after the stability test. Moreover, the amorphous structure and the sheet-like morphology could be well maintained after the *i-t* test (Fig. 5c and 5d), further demonstrating the excellent structural robustness.

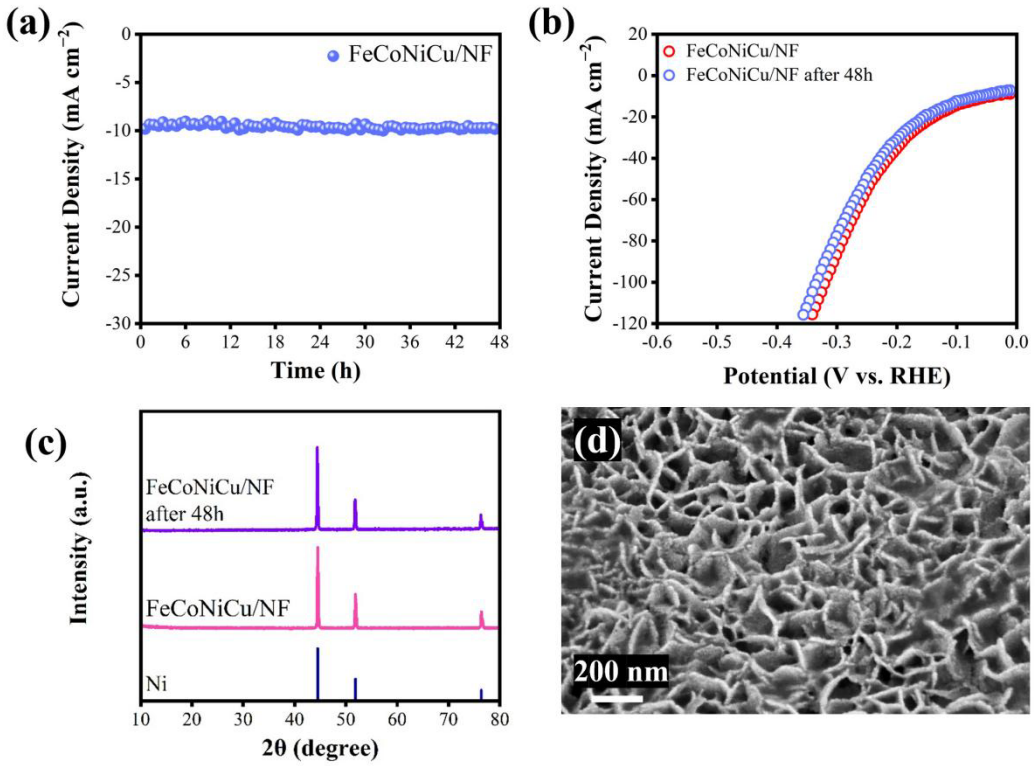

Fig. 5. (a) i-t curve of FeCoNiCu/NF. (b) LSV curves of FeCoNiCu/NF before and after long-term stability test. (c) XRD patterns of FeCoNiCu/NF before and after the i-t test. (d) FESEM image of FeCoNiCu/NF after the stability test.

To optimize the HER catalytic activity of as-fabricated electrocatalyst, controlled experiments with different electrochemical deposition potentials and durations were subsequently conducted. Fig. S9 (Supporting Information) shows the FESEM images of FeCoNiCu alloys deposited on the nickel foam at different electrodeposition potentials of −2.1 V, −2.3 V, −2.5 V and –2.7 V (vs. saturated calomel electrode [SCE]), respectively. It could be clearly observed that when the electrodeposition

potential was fixed at −2.1 V, only sparse nanosheets with tiny size were deposited on the substrate. As the decreasing electrodeposition potentials, vertically aligned nanosheets interconnect and become increasingly dense. When the electrodeposition potential becomes more negative than −2.5 V (including −2.5 V), a large number of metal ions is reduced, nanosheets cohere together and generated thick layers, which might be unfavorable to the exposure of catalytically active sites and the penetration of electrolyte. The electrochemical tests toward HER activity were subsequently carried out. As shown in Fig. S10 (Supporting Information), benefiting from the open voids and ultrathin sheet-like structure, the FeCoNiCu/NF obtained at −2.3 V exhibits the lowest overpotential of 35 mV at 10 mA cm^{-2}, the smallest Tafel slope of 57 mV dec^{-1} and charge transfer resistance of 14.6 Ω.

Apart from the deposition potentials, effects of the deposition time on the electrochemical performance were also studied with a fixed deposition potential of −2.3 V. Fig. S11, S12 and Table S5 (Supporting Information) display the integral charge and deposition quantity throughout the deposition processes. Accordingly, the quality of deposited alloys is directly proportional to the deposition time. The electrochemical HER performances of FeCoNiCu/NF electrodes deposited for 10, 15, 20 and 25 minutes were displayed in Fig. S13 (Supporting Information). Obviously, the electrochemical performances (evaluated by the overpotential, Tafel slope and charge transfer resistance) firstly exhibits an improved trend with the prolonged deposition process. But when the deposition time reaches 25 min, the electrochemical performance becomes worse because of the detrimental effects of excessive deposits on interlocking nanoplate structures, which could impede mass transfer channels during the HER process and lead to suboptimal catalytic activity.

4. Conclusion

In summary, a simple and efficient electrochemical deposition process was developed for synthesis of amorphous quaternary FeCoNiCu alloy nanosheets supported on the nickel foam. Vertically aligned and interconnected porous nanosheets lead to high exposure of active sites and abundant mass transfer channels. Along with the regulated electronic structure and optimal adsorption properties of intermediates derived from the synergy of multi-metal atoms interaction, the as-synthesized FeCoNiCu/NF electrode exhibits a low overpotential of 35 mV at a current density of 10 mA cm^{-2} toward HER in alkaline electrolyte and demonstrates exceptional stability without any noticeable degradation for up to 48 hours. This study may present a straightforward and energy-efficient approach for fabricating novel amorphous alloy catalysts that can be applied in HER and other electrochemical reactions involved in energy conversion processes.

Acknowledgements

This work was financially supported by "Shuguang Program" supported by Shanghai Education Development Foundation and Shanghai Municipal Education Commission (20SG03), Opening Project of State Key Laboratory of High Performance Ceramics and Superfine Microstructure (No. SKL202101SIC), and Science and Technology Commission of Shanghai Municipality (No. 22520710600).

References

[1] H. Zhang, Y. Luo, P.K. Chu, Q. Liu, X.J. Liu, S.S. Zhang, J. Luo, X.Z Wang, G.Z. Hu, Recent advances in non-noble metal-based bifunctional electrocatalysts for overall seawater splitting, Journal of Alloys and Compounds. 922 (2022) 166113.

[2] P.F. Guo, L.X. Shi, D. Liu, X.Q. Wang, F. Gao, Y. Ha, J. Yin, M. Liu, H.G. Pan, R.B. Wu, Fe-doping-induced cation substitution and anion vacancies promoting Co_3O_4 hexagonal nanosheets for efficient overall water splitting, Materials Today

Catalysis. 1 (2023) 100002.

[3] Z.L. Chen, H.L. Qing, K. Zhou, D.L. Sun, R.B. Wu, Metal-organic framework-derived nanocomposites for electrocatalytic hydrogen evolution reaction, Progress in Materials Science. 108 (2020) 100618.

[4] Z.X. Dai, X.Q. Du, X.S. Zhang, The synthesis of Ni-Co-Fe-Se@NiCo-LDH nanoarrays on Ni foam as efficient overall water splitting electrocatalyst, Journal of Alloys and Compounds. 946 (2023) 169451.

[5] J. Qu, Z.M. Wang, W.J. Gan, R. Xiao, X.C. Yao, Z. Khanam, L.Z. Ouyang, H. Wang, H. Yang, S.G. Zhang, M.S. Balogun, Efficient hydrogen evolution on antiperovskite $CuNCo_3$ nanowires by Mo incorporation and its trifunctionality for Zn air batteries and overall water splitting, Small, 9 (2023) 202304541.

[6] J. Chen, Y. Ha, R.R. Wang, Y.X. Liu, H.B. Xu, B. Shang, R.B. Wu, H.G. Pan, Inner Co synergizing outer Ru supported on carbon nanotubes for efficient pH-universal hydrogen evolution catalysis, Nano-Micro Letters. 14 (2022) 186.

[7] H.B. Xu, H.X. Jia, B. Fei, Y. Ha, H.Z. Li, Y.H. Guo, M. Liu, R.B. Wu, Charge transfer engineering via multiple heteroatoms doping in dual carbon-coupled cobalt phosphides for highly efficient overall water splitting, Applied Catalysis B: Environmental. 268 (2021) 118404.

[8] B. Fei, Z.L. Chen, J.X. Liu, H.B. Xu, X.X. Yan, H.L. Qing, M. Chen, R.B. Wu, Ultrathinning nickel sulfide with modulated electron density for efficient water splitting, Advanced Energy Materials. 10 (2020) 2001963.

[9] Z.M. Wang, J. Qu, Y.X. He, T.Z. Xiong, Z.M. Huang, F. Wang, M.S. Balogun, Exceptional alkaline hydrogen evolution by molybdenum-oxide-nitride-based electrocatalysts with fast water-dissociation and hydrogen-adsorption kinetics, Materials Chemistry Frontiers. 13 (2023) 2683-2692.

[10] F.B. Guo, X.Y. Zhao, J. Cheng, K.K. Liu, L.X. Zhang, Ni MOF-derived $MoSe_2$@$NiSe_2$ heterostructure with hollow core-shell for efficient hydrogen evolution reaction, Journal of Alloys and Compounds. 947 (2023) 169513.

[11] H.Y. Yang, J.X. Liu, Z.L. Chen, R.R. Wang, B. Fei, H.X. Liu, Y.H. Guo, R.B. Wu, Unconventional bi-vacancies activating inert Prussian blue analogues nanocubes for efficient hydrogen evolution, Chemical Engineering Journal. 420 (2021) 127671.

[12] W. Li, J. Liu, P.F. Guo, H.Z. Li, B. Fei, Y.H. Guo, H.G. Pan, D.L. Sun, F. Fang, R.B. Wu, Co/CoP heterojunction on hierarchically ordered porous carbon as a highly efficient electrocatalyst for hydrogen and oxygen evolution, Advanced Energy Materials. 11 (2021) 2102134.

[13] H.B. Zhang, X.Q. Du, X.S. Zhang, Y.H. Wang, Controlled synthesis of NiCoP@NiM LDH (M=Cu, Fe, Co) as efficient hydrogen evolution reaction electrocatalyst, Journal of Alloys and Compounds. 937 (2023) 168412.

[14] J.Y. Chen, Y.C. Ge, Q.Y. Feng, P.Y. Zhuang, H. Chu, Y.D. Cao, W.R. Smith, P. Dong, M.X. Ye, J.F. Shen, Nesting Co_3Mo binary alloy nanoparticles onto molybdenum oxide nanosheet arrays for superior hydrogen evolution reaction, ACS Applied Materials & Interfaces. 11 (2019) 9002–9010.

[15] I.S. Kwon, I.H. Kwak, G.M. Zewdie, S.J. Lee, J.Y. Kim, S.J. Yoo, J.G. Kim, J. Park, H.S. Kang, $MoSe_2$-VSe_2-$NbSe_2$ ternary alloy nanosheets to boost electrocatalytic hydrogen evolution reaction, Advanced Materials. 34 (2022) 2205524.

[16] G. Yan, H.Q. Tan, Y.H. Wang, Y.G. Li, Amorphous quaternary alloy phosphide hierarchical nanoarrays with pagoda-like structure grown on Ni foam as pH-universal electrocatalyst for hydrogen evolution reaction, Applied Surface Science. 489 (2019) 519–527.

[17] X. Wang, W. Guo, Y.Z. Fu, High-entropy alloys: emerging materials for

advanced functional applications, Journal of Materials Chemistry A. 9 (2021) 663–701.

[18] Z. Jia, T. Yang, L.G. Sun, Y.L. Zhao, W.P. Li, J.H. Luan, F.C. Lyu, L.C. Zhang, J.J. Kruzic, J.J. Kai, J.C. Huang, J. Lu, C.T. Liu, A novel multinary intermetallic as an active electrocatalyst for hydrogen evolution, Advanced Materials. 32 (2020) 2000385.

[19] P.Y. Ma, M.M. Zhao, L. Zhang, H. Wang, J.F. Gu, Y.C. Sun, W. Ji, Z.Y. Fu, Self-supported high-entropy alloy electrocatalyst for highly efficient H_2 evolution in acid condition, Journal of Materiomics. 6 (2020) 736–742.

[20] S.L. Yin, Z.Q. Wang, H.G. Zhang, C.J. Li, H.J. Yu, Y. Xu, X.N. Li, L. Wang, H.J. Wang, Enhancing hydrogen evolution activity of triangular PtPdCu nanodarts by phosphorus incorporation, Chemical Engineering Journal. 339 (2020) 125810.

[21] X. Cao, Y. Han, C.Z. Gao, Y. Xu, X.M. Huang, M. Willander, N. Wang, Highly catalytic active PtNiCu nanochains for hydrogen evolution reaction, Nano Energy. 9 (2014) 301–308.

[22] Z.J. Chen, T. Zhang, X.Y. Gao, Y.J. Huang, X.H. Qin, Y.F. Wang, K. Zhao, X. Peng, C. Zhang, L. Liu, M.H. Zeng, H.B. Yu, Engineering microdomains of oxides in high-entropy alloy electrodes toward efficient oxygen evolution, Advanced Materials. 33 (2021) 2101845.

[23] Q.R. Yao, Y.T. Zhou, H. Shi, W.B. Wan, Q.H. Zhang, L. Gu, Y.F. Zhu, Z. Wen, X.Y. Lang, Q. Jiang, Nanoporous surface high-entropy alloys as highly efficient multisite electrocatalysts for nonacidic hydrogen evolution reaction, Advanced Functional Materials. 31 (2020) 2009613.

[24] B.H.R. Suryanto, Y. Wang, R.K. Hocking, W. Adamson, C. Zhao, Overall electrochemical splitting of water at the heterogeneous interface of nickel and iron

oxide, Nature Communication. 10 (2019) 5599.

[25] S.W. Li, Y.C. Wang, S.J. Peng, L.J. Zhang, A.M. Al-Enizi, H. Zhang, X.H. Sun, G.F. Zheng, Co-Ni-based nanotubes/nanosheets as efficient water splitting electrocatalysts, Advanced Energy Materials. 6 (2016) 1501661.

[26] C.Z. Yao, P. Zhang, M. Liu, G.R. Li, J.Q. Ye, P. Liu, Y.X. Tong, Electrochemical preparation and magnetic study of Bi-Fe-Co-Ni-Mn high entropy alloy, Electrochimica Acta. 53 (2008) 8359–8365.

[27] X. Yang, Y. Zhang, Prediction of high-entropy stabilized solid-solution in multi-component alloys, Materials Chemistry and Physics, 132 (2012) 233–238.

[28] W.A. Saidi, W. Shadid, G. Veser, Optimization of high-entropy alloy catalyst for ammonia decomposition and ammonia synthesis, Journal of Physical Chemistry Letters. 12 (2021) 5185–5192.

[29] D. Zhang, Y. Shi, H. Zhao, W.J. Qi, X.L. Chen, T.R. Zhan, S.X. Li, B. Yang, M.Z. Sun, J.P. Lai, B.L. Huang, L. Wang, The facile oil-phase synthesis of a multi-site synergistic high-entropy alloy to promote the alkaline hydrogen evolution reaction, Journal of Materials Chemistry A. 9 (2021) 889–893.

[30] H.J. Qiu, G. Fang, J.J. Gao, Y.R. Wen, J. Lv, H.L. Li, G.D. Xie, X.J. Liu, S.H. Sun, Noble metal-free nanoporous high-entropy alloys as highly efficient electrocatalysts for oxygen evolution reaction, ACS Materials Letters. 1 (2019) 526–533.

[31] Y.T. Hsiao, C.H. Tung, S.J. Lin, J.W. Yeh, S.Y. Chang, Thermodynamic route for self-forming 1.5 nm V-Nb-Mo-Ta-W high-entropy alloy barrier layer: roles of enthalpy and mixing entropy, Acta Materialia. 199 (2020) 107–115.

[32] Y. Zhang, T.T. Zuo, Z. Tang, M.C. Gao, K.A. Dahmen, P.K. Liaw, Z.P. Lu, Microstructures and properties of high-entropy alloys, Progress in Materials Science.

61 (2014) 1–93.

[33] J.Y. Chen, Y.C. Ge, Q.Y. Feng, P.Y. Zhuang, H. Chu, Y.D. Cao, W.R. Smith, P. Dong, M.X. Ye, J.F. Shen, Nesting Co_3Mo binary alloy nanoparticles onto molybdenum oxide nanosheet arrays for superior hydrogen evolution reaction, ACS Applied Materials & Interfaces. 11 (2019) 9002–9010.

[34] X.D. Zhang, Y. Li, Y.K. Guo, A.M. Hu, M. Li, T. Hang, H.Q. Ling, 3D hierarchical nanostructured Ni-Co alloy electrodes on porous nickel for hydrogen evolution reaction, International Journal of Hydrogen Energy. 44 (2019) 29946–29955.

[35] J. Cao, H.C. Li, J.X. Pu, S.C. Zeng, L.M. Liu, L. Zhang, F.H. Luo, L. Ma, K.C. Zhou, Q.P. Wei, Hierarchical NiMo alloy microtubes on nickel foam as an efficient electrocatalyst for hydrogen evolution reaction, International Journal of Hydrogen Energy. 44 (2019) 24712–24718.

[36] T.T. Sun, J. Cao, J. Dong, H.Y. Du, H.J. Zhang, J.F. Chen, L.B. Xu, Ordered mesoporous Ni-Co alloys for highly efficient electrocatalytic hydrogen evolution reaction, International Journal of Hydrogen Energy. 42 (2017) 6637–6645.

[37] J.W. Zhang, J.T. Huang, K. Wang, Y. Gao, S. Lou, F. Zhou, S.C. Yan, Synthesis of Co_2FeAl alloys as highly efficient electrocatalysts for alkaline hydrogen evolution reaction, International Journal of Hydrogen Energy. 47 (2022) 13399–13408.

[38] Y. Jia, X.H. Gao, C.Q. Teng, X.Y. Li, Y. Liu, M.J. Zhi, Z.L. Hong, Co_2Ni alloy/N-doped CNTs composite as efficient hydrogen evolution reaction catalyst in alkaline medium, Journal of Alloys and Compounds. 791 (2019) 779–785.

[39] S. Saha, S. Vaidya, K.V. Ramanujachary, S.E. Lofland, A.K. Ganguli, Ternary alloy nanocatalysts for hydrogen evolution reaction, Bulletin of Materials Science. 39 (2016) 433–436.

[40] Y. Yang, Z.Y. Lin, S.Q. Gao, J.W. Su, Z.Y. Lun, G.L. Xia, J.T. Chen, R.R. Zhang, Q.W. Chen, Tuning electronic structures of nonprecious ternary alloys encapsulated in graphene layers for optimizing overall water splitting activity, ACS Catalysis. 7 (2017) 469–479.

[41] D. Gao, J.N. Guo, X. Cui, L. Yang, Y. Yang, H.C. He, P. Xiao, Y.H. Zhang, Three-dimensional dendritic structures of NiCoMo as efficient electrocatalysts for the hydrogen evolution reaction, ACS Applied Materials & Interfaces. 9 (2017) 22420–22431.

[42] F.N. Wang, Y.M. Sun, Y.H. He, L.H. Liu, J.M. Xu, X.C. Zhao, G.Z. Yin, L.P. Zhang, S.Z. Li, Q. Mao, Y.Q. Huang, T. Zhang, Highly efficient and durable MoNiNC catalyst for hydrogen evolution reaction, Nano Energy. 37 (2017) 1–6.

[43] G.L. Zhang, K.S. Ming, J.L. Kang, Q. Huang, Z.J. Zhang, X.R. Zheng, X.F. Bi, High entropy alloy as a highly active and stable electrocatalyst for hydrogen evolution reaction, Electrochemica Acta. 279 (2018) 19–23.

[44] J. Park, H. Kim, S.Y. Kim, S.H. Ahn, Empirical approach for configuring high-entropy catalysts in alkaline water electrolysis, International Journal of Energy Research. 46 (2022) 9938–9947.

[45] Y. Wang, B. Yu, M. He, Z.H. Zhai, K.B. Yin, F.G. Kong, Z.H. Zhang, Eutectic-derived high-entropy nanoporous nanowires for efficient and stable water-to-hydrogen conversion, Nano Research. 15 (2022) 4820–4826.

[46] N. Lotfi, T. Shahrabi, Y. Yaghoubinezhad, G.B. Darband, Direct electrodeposition of platinum nanoparticles@graphene oxide@nickel-copper@nickel foam electrode as a durable and cost-effective catalyst with remarkable performance for electrochemical hydrogen evolution reaction, Applied Surface Science. 505 (2020) 144571.